

Enhancing Triple Negative Breast Cancer Immunotherapy by ICG-Templated Self-Assembly of Paclitaxel Nanoparticles

Bing Feng, Zifei Niu, Bo Hou, Lei Zhou, Yaping Li,* and Haijun Yu*

Combination cancer immunotherapy has shown promising potential for simultaneously eliciting antitumor immunity and modulating the immunosuppressive tumor microenvironment (ITM). However, combination immunotherapy with multiple regimens suffers from the varied chemo-physical properties and inconsistent pharmacokinetic profiles of the different therapeutics. To achieve tumor-specific codelivery of the immune modulators, an indocyanine green (ICG)-templated self-assembly strategy for preparing dual drug-loaded two-in-one nanomedicine is reported. ICG-templated self-assembly of paclitaxel (PTX) nanoparticles (ISPN), and the application of ISPN for combination immunotherapy of the triple negative breast cancer (TNBC) are demonstrated. The ISPN show satisfied colloidal stability and high efficacy for tumor-specific codelivery of ICG and PTX through the enhanced tumor permeability and retention effect. Upon laser irradiation, the ICG component of ISPN highly efficiently induces immunogenic cell death of the tumor cells via activating antitumor immune response through photodynamic therapy. Meanwhile, PTX delivered by ISPN suppresses the regulatory T lymphocytes (T_{reg} s) to combat ITM. The combination treatment of TNBC with ISPN and α PD-L1-mediated immune checkpoint blockade therapy displays a synergistic effect on tumor regression, metastasis inhibition, and recurrence prevention. Overall, the ICG-templated nanomedicine may represent a robust nanoplatform for combination immunotherapy.

1. Introduction

Triple negative breast cancer (TNBC) represents one of the most malignant tumors with highly invasive and metastatic features.^[1–3] Chemotherapy is the major approach for clinical therapy of the advanced or metastatic TNBC tumors. However, chemotherapy displays limited therapeutic benefits due to the occurrence of the intrinsic or acquired multiple drug resistance.^[4–6] In past few years, immunotherapy, in particular, immune checkpoint blockade (ICB)


therapy has ushered a new chapter for cancer therapy to elicit durable antitumor response and dramatically lengthen the surveillance of cancer patients.^[7–9] Despite promising, the TNBC patients rarely benefit from current ICB therapy due to low immunogenicity and immunosuppressive tumor microenvironment (ITM) of TNBC tumors.^[10–16] Thus, complementary approaches to enhance the immunogenicity and reverse the ITM remain a formidable challenge for improving immunotherapy of TNBC.^[17–20]

The combination of ICB therapy with chemotherapy, photodynamic therapy (PDT) or radiotherapy has displayed synergistic antitumor effect to facilitate intratumoral infiltration of cytotoxic T lymphocytes (CTLs) and overcome the ITM.^[21–26] However, combination immunotherapy suffers from the distinct chemo-physical properties and inconsistent pharmacokinetic profiles of the different immune modulators. Despite nanoparticle-based drug delivery systems show promising potential for combination immunotherapy by integrating multiple regimens into one single nanoplatform, the preparation schemes of current

nanomedicine are generally too complicated to achieve reproductivity and quality control.^[27,28] Moreover, excipients are essential for preparing drug-loaded nanoparticles, which cause unsatisfied drug loading ratios.^[29,30] In recent years, excipient-free nanomedicines have attracted extensive attention for highly efficient drug delivery.^[31–34] Most of current excipient-free nanomedicines have been designed as prodrug structures to self-assemble into nanoformulations.^[35–37] Chemical modification of the small molecular therapeutics are essential for developing conventional excipient-free nanoparticles, which might impair the therapeutic performance of the anticancer drugs.^[38–40]

To this end, we herein reported a robust approach, so called indocyanine green (ICG)-templated self-assembly strategy for preparing two-in-one nanomedicine and combination immunotherapy. Such a procedure can achieve nearly 100% loading of a large variety of the small molecular drugs without the use of any excipients (Figure 1a). For proof-of-concept, we focused on the development of ICG-templated self-assembly of Paclitaxel (PTX) nanoparticles (termed as ISPN) for combination immunotherapy of TNBC (Figure 1b). ICG can perform PDT to induce immunogenic cell death (ICD) of the tumor cells.^[41–44] Tumor cells undergoing ICD expose the calreticulin (CRT)

Dr. B. Feng, Z. Niu, B. Hou, L. Zhou, Prof. Y. Li, Prof. H. Yu
State Key Laboratory of Drug Research & Center of Pharmaceutics
Shanghai Institute of Materia Medica
Chinese Academy of Sciences
Shanghai 201203, China
E-mail: ypli@simm.ac.cn; hjyu@simm.ac.cn
B. Feng, Y. Li, H. Yu
University of Chinese Academy of Sciences
Beijing 100049, China

 The ORCID identification number(s) for the author(s) of this article can be found under <https://doi.org/10.1002/adfm.201906605>.

DOI: 10.1002/adfm.201906605

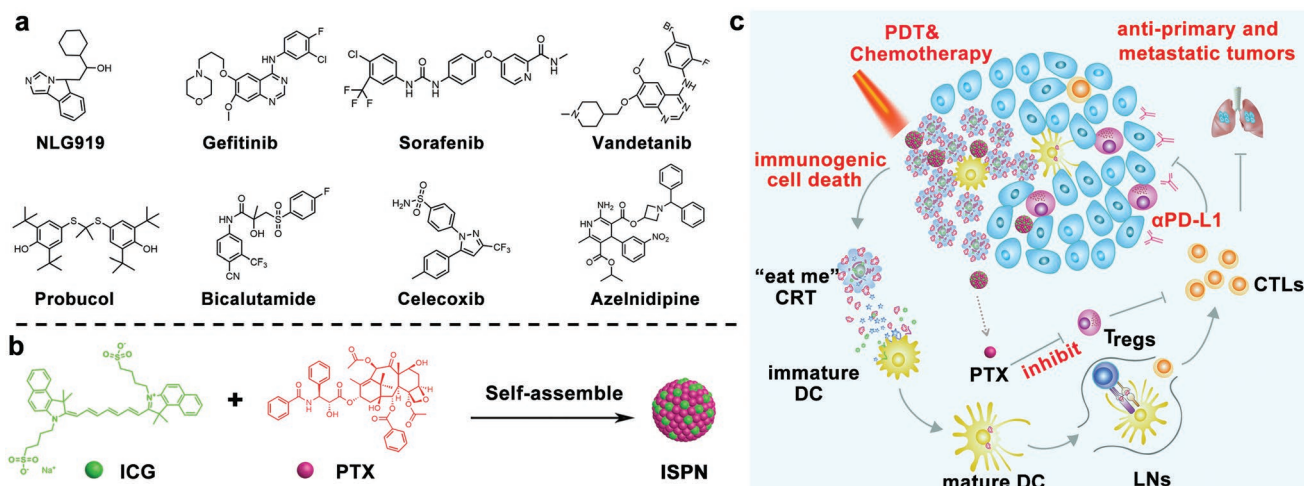


Figure 1. Schematic illustration of ICG-templated self-assembly of PTX nanoparticles for immunotherapy of TNBC tumors. a) A library of small molecular drugs screened for ICG-templated self-assembly strategy; b) ICG-templated self-assembly of PTX nanoparticles; c) Schematic illustration of ISPN-mediated cancer immunotherapy by combining with ICB for inducing ICD of the tumor cells and eliminating immunosuppressive T_{regs} .

on the surface of cell membrane, release high mobility group box 1 (HMGB1), and secrete adenosine triphosphate (ATP) for priming antitumor immune response.^[45–47] Meanwhile, PTX, delivered with ISPN to combat ITM by specifically killing the regulatory T cells (T_{regs}). PTX is one of the first-line chemotherapeutics for clinical TNBC treatment, which suppresses tumor growth by stabilizing the microtubule and inhibiting mitosis of the tumor cells. Along with the chemo-cytotoxicity of PTX, several preclinical and clinical studies suggested that PTX enhances the therapeutic performance of ICB therapy by modulating the immunosuppressive tumor microenvironment.^[48–55] For instance, low dose of PTX (5 mg kg^{-1}) efficiently reversed ITM by down-regulating T_{regs} . PTX reduces the fraction of intratumorally infiltrating T_{regs} and suppresses the immune inhibitory function of T_{regs} by upregulating cell death receptor Fas (also known as CD95).^[56,57] In combination with the immune checkpoint inhibitor (i.e., anti-PD-L1 antibody, $\alpha\text{PD-L1}$), ISPN displayed synergistic antitumor performance in TNBC tumor-bearing immunocompetent mouse model (Figure 1c). Overall, ICG-templated self-assembly nanomedicine might represent a robust strategy for TNBC immunotherapy.

2. Results and Discussion

2.1. Preparation and Characterization of ICG-Templated Nanomedicine

To demonstrate the generality of ICG-templated self-assembly strategy, we screened a library of small molecular drugs including kinase inhibitors (e.g., Gefitinib, Sorafenib, Vandetanib, and Celecoxib), androgen receptor antagonist (e.g., Bicalutamide), calcium channel blocker (e.g., Azelidipine), antihyperlipidemic drug (e.g., Probuocol), chemotherapeutics (e.g., Paclitaxel and Docetaxel), and immune regulator (e.g., NLG919). All these drugs formed stable nanoparticle with ICG, implying the promising potential of ICG-templated self-assembly strategy for highly efficient encapsulation of a large

variety of the small molecular therapeutics (Figure S1, Supporting Information).

To fabricate ISPN, 0.8 mg of PTX in 100 μL of dimethylsulfoxide (DMSO) was mixed with the aqueous solution of ICG (1 mg mL^{-1}) under constant shaking. ISPN was purified by centrifugation and ultrafiltration, which was redispersed in deionized (DI) water. The PTX and ICG loading rates were determined to be $\approx 90.7\%$ and 9.2% , respectively. The encapsulation efficacy of PTX and ICG were $81.9 \pm 11.9\%$ and $4.9 \pm 0.5\%$, respectively, as determined by high performance liquid chromatography (HPLC) measurement.

ISPN showed a hydrodynamic diameter of $112 \pm 1.06 \text{ nm}$ (polydispersity index, PDI = 0.1) and a negative surface charge (-34.5 mV) as examined by dynamic light scattering (DLS) measurement (Figure 2a). Transmission electron microscopic (TEM) examination further revealed uniformed particles size and spherical morphology of ISPN (Figure 2b). ISPN displayed good colloidal stability in both phosphate buffer solution (PBS) for 7 d (Figure 2c and Figure S2, Supporting Information). ISPN kept consistent hydrodynamic particle size around 121 nm when the PTX concentration was serially diluted from $100 \mu\text{g mL}^{-1}$ to as low as $1.0 \mu\text{g mL}^{-1}$ in PBS, further verifying good colloidal stability of ISPN (Figure 2d). ISPN could be lyophilized and readily redispersed in DI water with slight particle size change, implying the potential of ISPN for long-term storage (Figure 2e,f).

To clarify the interaction between ICG and PTX, we incubated the ISPN nanoparticles with sodium dodecyl sulfate (SDS), urea and NaCl, respectively. The photoabsorption spectrum of ISPN remained unchanged after the addition of NaCl and urea with a maximum peak at 784 nm. In contrast, the maximum absorption peak of ICG shifted to 795 nm when incubated with SDS, as same as that of free ICG dissolved in DMSO (Figure 2g). The crystallization of PTX in ISPN was examined using differential scanning calorimeter measurement. Much lower crystallization degree of PTX was found in ISPN than that of free PTX, indicating the formation of tiny PTX crystals in ISPN. This can be attributed to the hydrophobic interaction between ICG-PTX, which hinders the crystallization of PTX (Figure S3, Supporting Information).

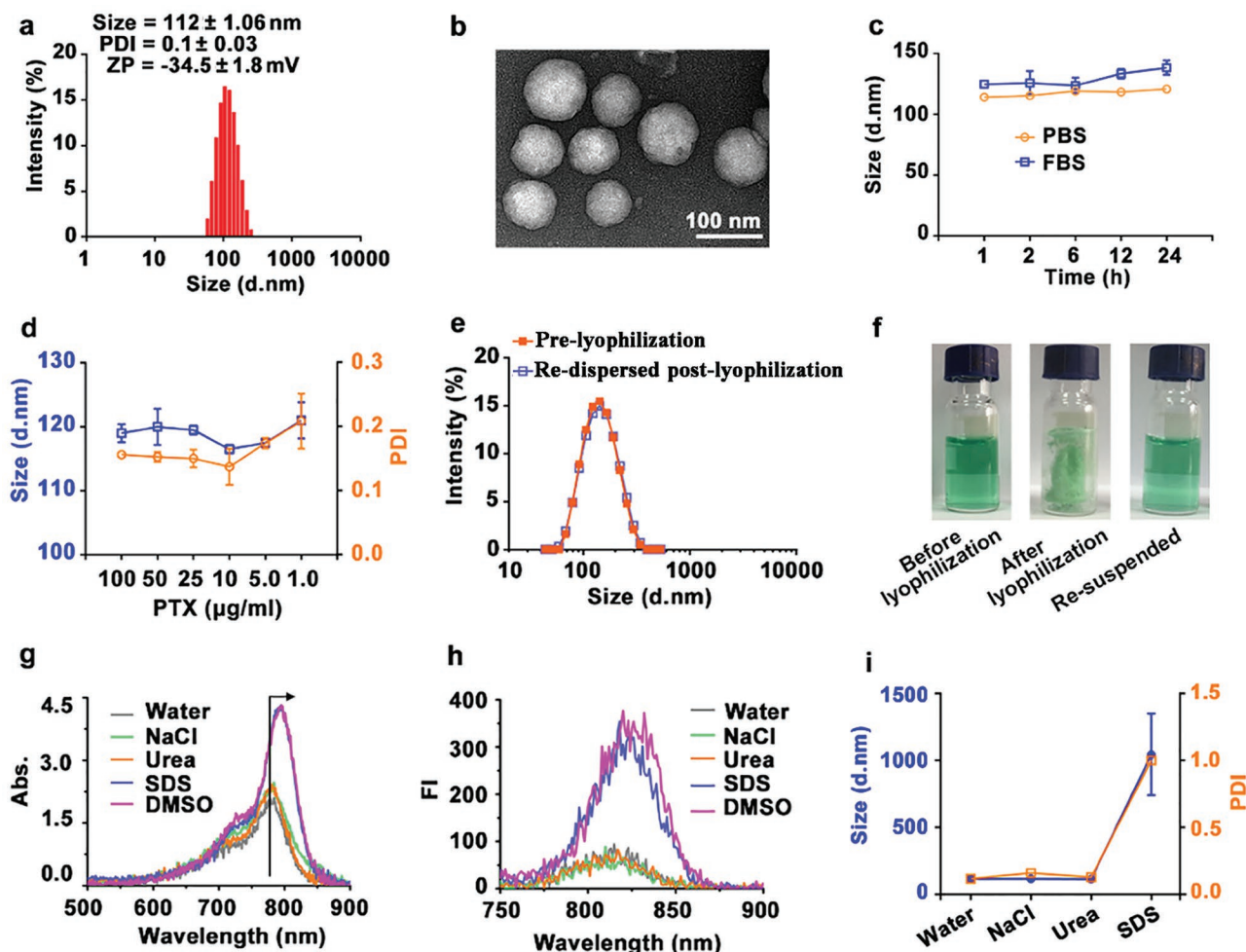


Figure 2. Physicochemical characterization of ISPN. a) Hydrodynamic diameter, and b) the representative TEM image (scale bar = 100 nm) of ISPN; c) the stability of ISPN in PBS or medium containing serum; d) The size change of ISPN during dilution up to $1.0 \mu\text{g mL}^{-1}$ of PTX; e) The size distribution of ISPN re-suspended in water after lyophilization; f) The respective image of ISPN solution before lyophilization, ISPN powder after lyophilization in 5% sucrose and ISPN resuspended in water; g) The UV spectrum, h) FI spectrum, i) and size change of ISPN in different buffer solutions.

ISPN displayed quenched fluorescent property as ICG aggregated to form nanoparticles with PTX. The fluorescence recovered with the addition of SDS but not urea or NaCl (Figure 2h). The absorption and fluorescence data both indicated SDS could effectively disassociate ISPN. SDS-induced ISPN dissociation was further verified by DLS examination. The particle size and polydispersity of the ISPN increased dramatically in the presence of SDS, suggesting hydrophobic interaction might be the dominant force for ICG-templated self-assembly of PTX (Figure 2i).

2.2. Cellular Uptake and Photoactivity of ISPN In Vitro

The cellular uptake of ISPN in vitro was examined in 4T1 tumor cells by flow cytometric measurement. ISPN showed increased cellular uptake than free ICG after incubation for different time. The intracellular fluorescence intensity of ISPN group was 2.1-fold higher than that of the ICG group after 8 h incubation, implying nanoparticulate formulation increased the cellular uptake of ICG (Figure 3a).

We next evaluated the photoactivity of ISPN in vitro by examining laser irradiation-induced generation of reactive oxygen species (ROS) with a ROS probe 2',7'-dichlorofluorescein diacetate (DCFH-DA), which could be converted into DCF with green fluorescence. After incubation with ISPN or ICG for 8 h at an identical ICG concentration of $1.0 \mu\text{g mL}^{-1}$, the cells were illuminated with 808 nm laser for 30 s at photodensity of 1.0 W cm^{-2} . Confocal laser scanning microscopic (CLSM) examination showed that more brilliant cellular red and green fluorescence assigned to ICG and DCF, respectively, could be observed in the cells incubated with ISPN after laser irradiation, which suggested the efficient cellular uptake and photoactivity of ISPN (Figure 3b).

2.3. Immunogenic Cell Death Induction of ISPN In Vitro

The intracellular DCF fluorescence intensity was further quantitatively determined by using flow cytometric examination. The ISPN+L group showed 2.7-fold higher intracellular DCF fluorescence intensity than that of the ICG group, implying

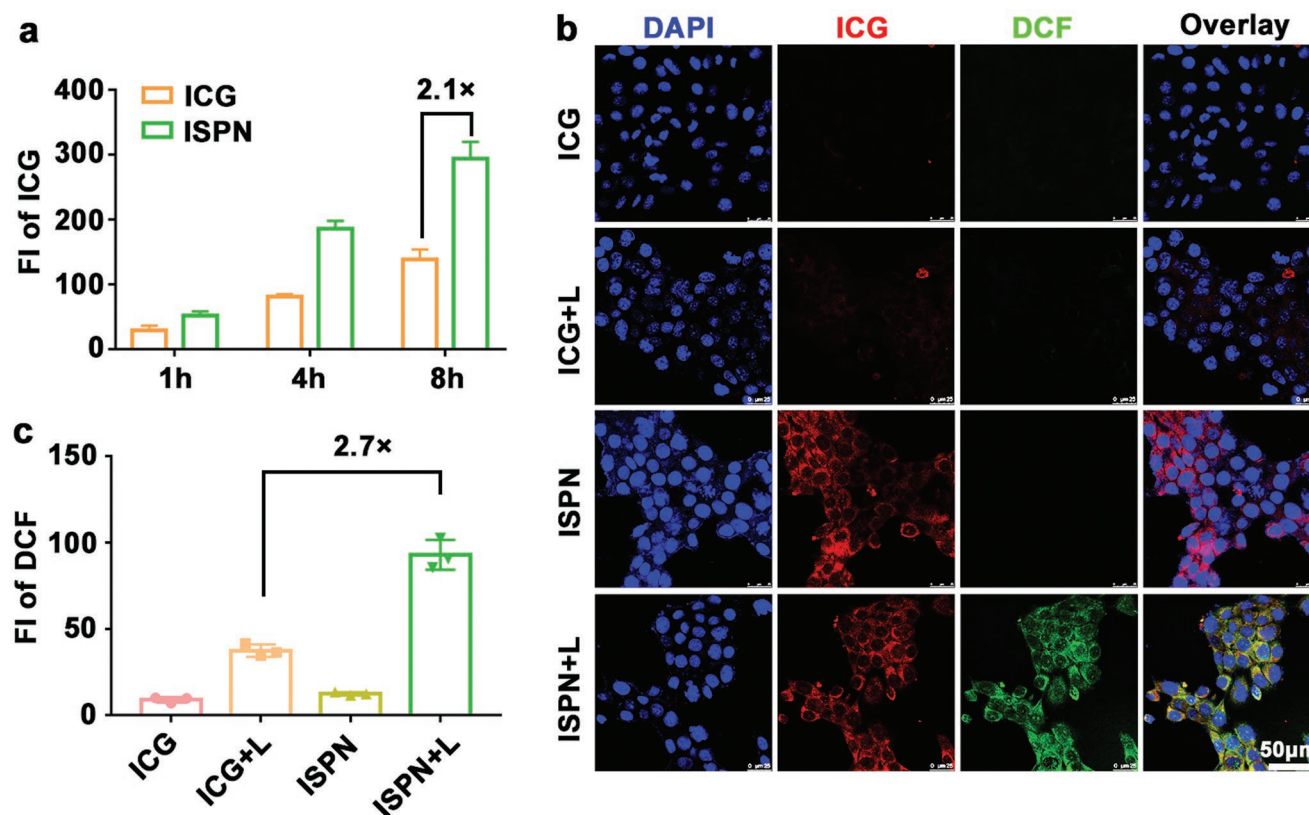


Figure 3. Cellular uptake and ROS production in vitro. a) Flow cytometric measurement of intracellular uptake of ISPN after incubation for different time; b) CLSM examination of intracellular distribution and ROS production of ISPN in 4T1 cells in vitro (Scale bar = 50 μm , photodensity of 1 W cm^{-2} , 30 s); c) Flow cytometric measurement of the cellular ROS production of ISPN in vitro after laser irradiation (photodensity of 1.0 W cm^{-2} , 30 s).

improved PDT effect of ISPN (Figure 3c). This could be attributed to the increased ICG uptake of ISPN group.

CRT has been defined as the dominant biomarker of ICD, which acts as a “eat me” signal to induce phagocytosis of the dying tumor cells by the antigen-presentation cells (e.g., dendritic cells, DCs).^[58] The endoplasmic reticulum stress caused by intracellular ROS generation could trigger CRT expression and transportation onto the surface of the tumor cells.^[59] To investigate the ICD induction profile of ISPN in vitro, 4T1 tumor cells were incubated with ISPN for 8 h at an ICG concentration of 1.0 $\mu\text{g mL}^{-1}$, the cells were then illuminated with 808 nm laser for 30 s at photodensity of 1.0 W cm^{-2} . The CRT expression on the surface of the tumor cells were examined 2 h postlaser illumination by using CLSM and flow cytometric measurements, respectively.

Figure 4a showed that ICG+L and ISPN both induced moderate CRT upregulation on the surface of 4T1 cells. In contrast, ISPN+L dramatically elicited CRT expression, as verified by flow cytometric measurement. For instance, ISPN+L group showed 2.0-fold higher CRT expression than that of the ICG+L group, which could be attributed to massive cellular ROS production by ISPN +L (Figure 4b,c).

We next examined treatment-induced translocation of protein HMGB1 from nucleus to extracellular matrix by immunofluorescence analysis. HMGB1 normally distributes in the nucleus of the normal cells, which migrates outside of the cell when the tumor cells undergo ICD. Extracellular HMGB1 can act as a Toll-like receptor agonist to stimulate DC maturation.

CLSM measurement showed complete HMGB1 migration out of the tumor cells (Figure 4d). Flow cytometric examination further revealed significant decline of HMGB1-positive 4T1 cells when the cells were treated with ISPN. Laser irradiation of the ISPN-treated cells further reduced the HMGB1-positive percentage to <7.4% (Figure 4e).

ATP secretion was evaluated by ATP assay to further verify the ICD induction property of ISPN. We found the ATP secretion in the cell culture medium of ISPN+L group was $39.6 \pm 3.3 \times 10^{-9}$ M with 2.6-fold and 2.1-fold higher than that of ICG+L and ISPN group, respectively (Figure 4f). These results suggested that ISPN could be efficiently uptake by tumor cells to induce the ICD of tumor cells through PDT.

Given the satisfied ICD-induction profile of ISPN, we next sought to evaluate ISPN-induced immunogenicity of the tumor cells by examining their impact on DC maturation in vitro. Immature DCs were freshly separated from BALB/c mice and incubated with the pretreated tumor cells for 24 h. The DC maturation was evaluated using flow cytometric measurement. Figure 4g displayed that tumor cells pretreated with ISPN+L significantly promoted DC maturation. The DC maturation frequency ($\text{CD11c}^+\text{CD80}^+\text{CD86}^+$) of the ISPN group was $\approx 18.6\%$, which dramatically increased to $\approx 50.1\%$ when the tumor cells were pretreated with laser illumination (Figure 4h). These results indicated that ISPN efficiently induced the ICD of tumor cells and enhanced the tumor immunogenicity for promoting DC maturation.

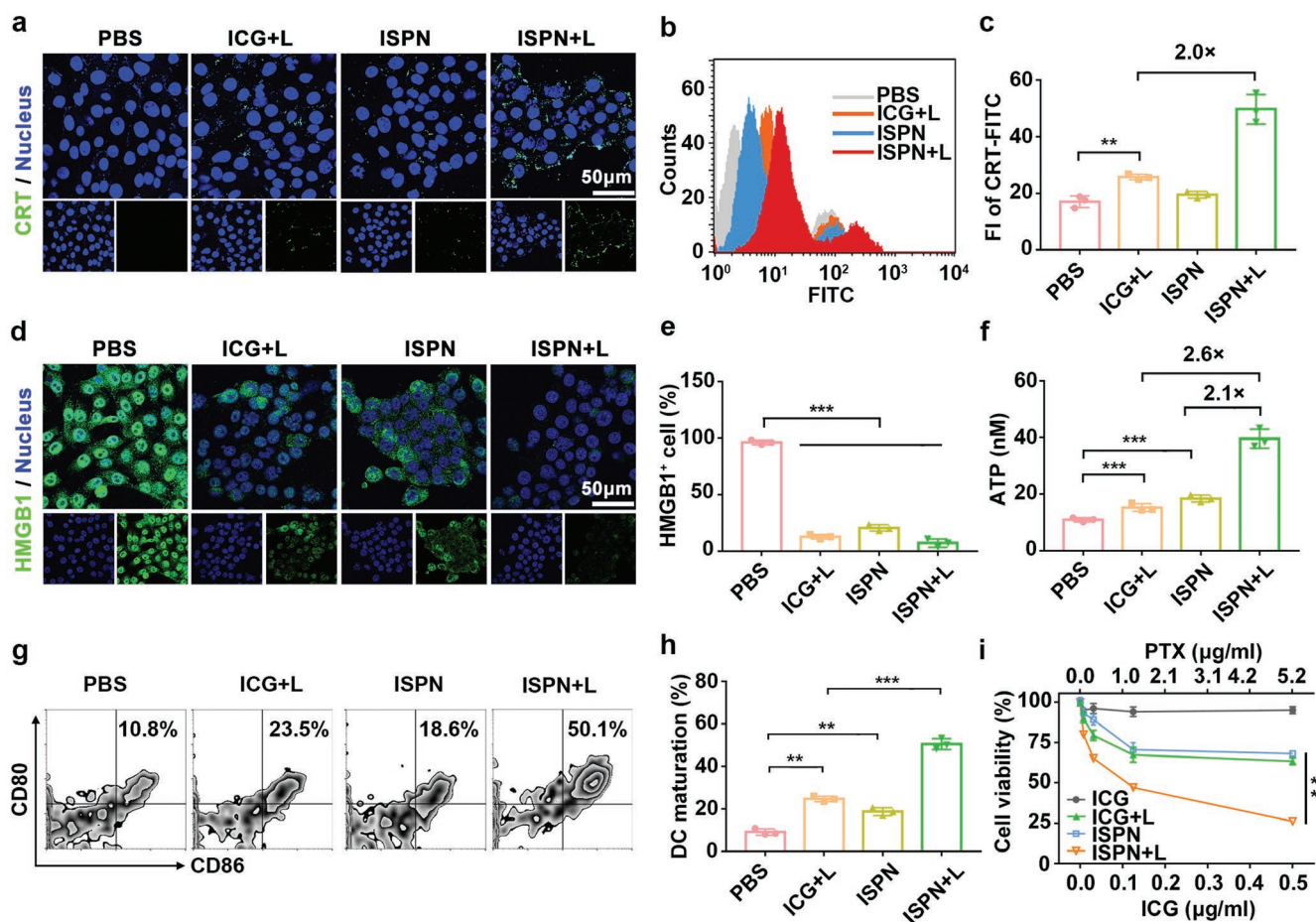


Figure 4. ICD induction effect of ISPN in vitro. a) CLSM, and b) flow cytometric measurement of CRT distribution on the surface of 4T1 tumor cells post ISPN-treatment and laser irradiation (photodensity of 1.0 W cm^{-2} , 30 s); c) Flow cytometric examination-determined CRT expression on the surface 4T1 cells; d) CLSM and e) flow cytometric examinations of HMGB1 release in ISPN-treated 4T1 cells; f) the ATP secretion in ISPN-treated 4T1 cells; g) Flow cytometric plots of BMDC maturation induced with ISPN-treated 4T1 cells (gated on CD11c^+); h) Flow cytometry determined BMDC maturation ratios; i) Cytotoxicity assay of ISPN in 4T1 cells in vitro (scale bar = $50 \mu\text{m}$, * $p < 0.05$; ** $p < 0.01$; *** $p < 0.001$).

The cytotoxicity of ISPN in 4T1 tumor cells was investigated in vitro. PDT therapy based on ICG and chemotherapy based on PTX caused moderate tumor cell death. In contrast, the cell viability significantly reduced by combination treated with ISPN and laser irradiation, indicating cumulative antitumor effect of ISPN-mediated chemotherapy and PDT in vitro (Figure 4i). We further compared the cytotoxicity of Liposome-PTX and ISPN in 4T1 tumor cells and found comparable IC_{50} of Lip-PTX and ISPN was 4.2 and $7.7 \mu\text{g mL}^{-1}$, respectively (Figure S4, Supporting Information).

2.4. Biodistribution of ISPN In Vivo

The biodistribution of ISPN was evaluated in 4T1 tumor bearing BALB/c mice. When the tumor volume reached 100 mm^3 , the tumor bearing mice was intravenously (i.v.) injected with ISPN at an ICG dose of 0.5 mg kg^{-1} . The biodistribution of ISPN was then examined using fluorescence imaging at the desired time points. Figure 5a displayed obvious

fluorescence signal in the tumor regions of the ISPN group, the fluorescence intensity reached the peak 4.5 h postinjection (Figure 5b). The mice were sacrificed 24 h postinjection for fluorescence imaging ex vivo (Figure 5c). The fluorescence signal of the ISPN group in tumors was 15.9-fold higher than that of ICG group (Figure 5d).

The PTX content within tumors was further determined by using HPLC examination. PTX solution was prepared by following a reported procedure.^[60–62] Briefly, PTX was dissolved in the mixed solvent of polyoxyethylated castor oil (Cremophor EL) and anhydrous ethanol (1:1, v/v) and then added into saline solution to obtain PTX solution at a cremophor/ethanol/saline volume ratio of 1/1/8. Free PTX and ISPN were then i.v. injected into the tumor bearing mice at an identical PTX dose of 5.0 mg kg^{-1} . The intratumoral PTX concentration of the ISPN group reached 23.5 mg kg^{-1} when examined 24 h postinjection, which was 11.2-fold higher than that of free PTX group (Figure 5e). The fluorescence imaging and PTX distribution data consistently verified ISPN facilitated the tumor accumulation of ICG and PTX through the EPR effect.

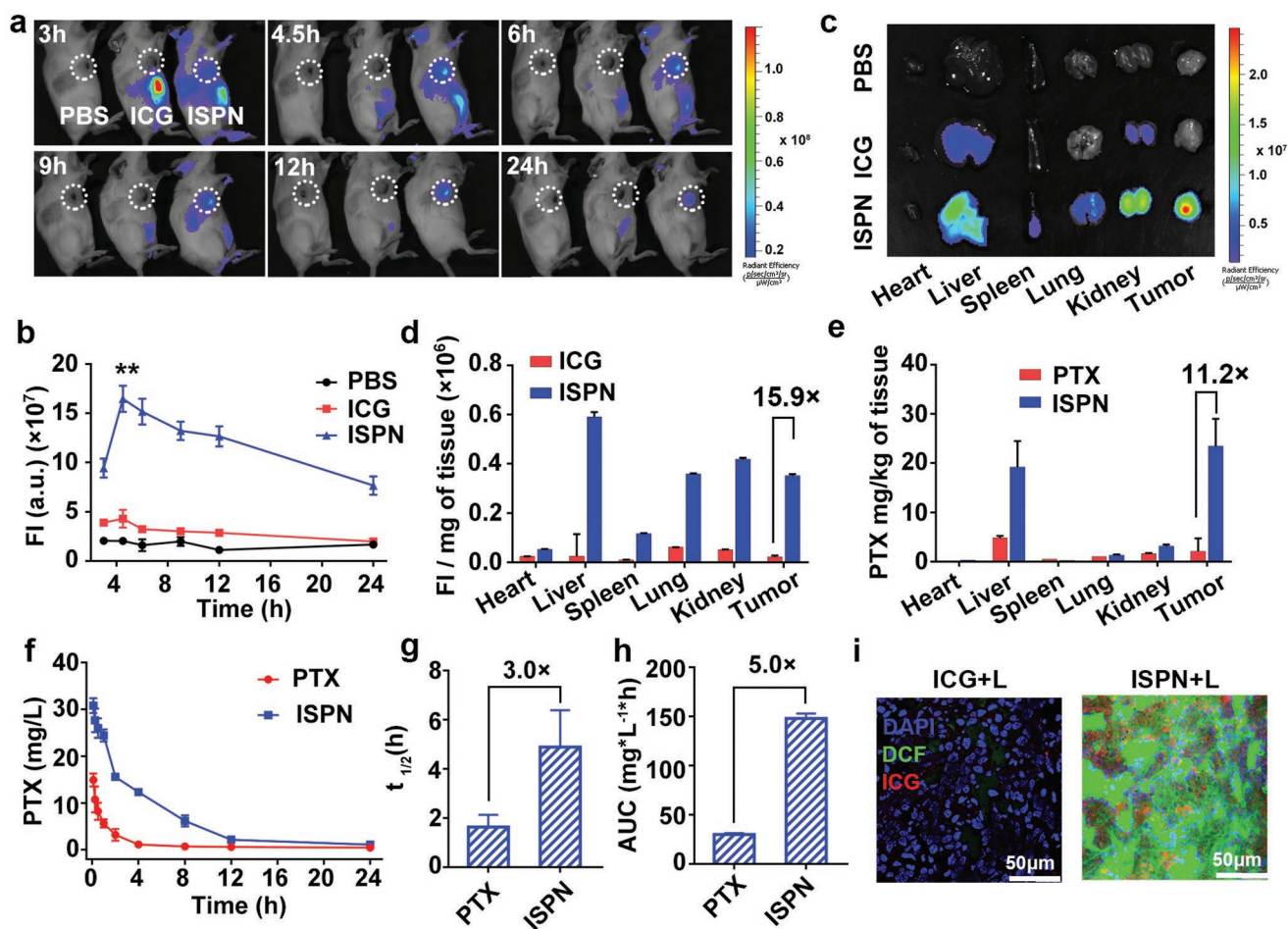


Figure 5. Biodistribution and pharmacokinetics profile of ISPN in vivo. a) Fluorescence imaging, and b) Semiquantitative fluorescence intensity of ISPN distribution in 4T1 tumor-bearing mice in vivo; c) Fluorescence imaging ex vivo, and d) the fluorescence intensity of the tumor organs examined 24 h postinjection; e) HPLC examination determined organ distribution of PTX in vivo; f) Plasma concentration-time profiles, g) Clearance half-life ($t_{1/2}$), and h) the area under curves (AUC_{0-24}) of PTX in SD rat post i.v. injection of ISPN or PTX; i) CLSM examination of laser-induced intratumoral ROS generation of ISPN + laser irradiation-treated 4T1 tumor-bearing BALB/c mice in vivo (Scale bars = 50 μm , $*p < 0.05$; $**p < 0.01$).

The pharmacokinetic profile of ISPN was then evaluated in Sprague Dawley (SD) rat. Figure 5f showed that free PTX was quickly eliminated after i.v. injection. In contrast, ISPN showed largely elongated blood circulation time (Figure 5g). The blood clearance half time ($t_{1/2}$) and area under curves (AUC_{0-24}) of ISPN was three- and fivefold higher than those of free PTX, respectively, verifying the excellent blood stability and pharmacokinetic profiles of ISPN (Figure 5h).

To determine laser irradiation-induced ROS generation in vivo, 4.5 h post ISPN injection, the 4T1 tumor-bearing mice were irradiated with 808 nm laser at photodensity of 2.0 W cm^{-2} for 5 min. The ROS probe DCFH-DA was intratumorally injected 20 min before laser irradiation. The tumors were collected immediately postlaser irradiation, frozen-sectioned, and stained with DAPI to examine ROS generation through CLSM. Fluorescence signal assigned to ICG (red) and DCF (green) of the ISPN group diffused throughout the tumor section, indicating ISPN could achieve efficient drug delivery and produce massive ROS in the tumor mass upon laser irradiation (Figure 5i).

2.5. Antitumor Efficacy of ISPN in Combination with ICB Therapy

Given the passive tumor targeting ability of ISPN, we next explored its potential for immunotherapy of TNBC. A typical TNBC murine tumor model was established by s.c. injecting 1×10^6 4T1 cells into the fat pad of BALB/c mice. When the tumor volume reached 100 mm^3 , the tumor bearing mice were randomly grouped ($n = 6$) and i.v. injected with ISPN or ICG at an identical ICG dose of 0.5 mg kg^{-1} and PTX dose of 5.0 mg kg^{-1} , respectively. The mice were then irradiated with 808 nm laser 4.5 h postinjection at photodensity of 2.0 W cm^{-2} for 5 min. Anti-PD-L1 antibody ($\alpha\text{PD-L1}$) was i.v. injected 24 h postlaser irradiation at a dose of 1.0 mg kg^{-1} (Figure 6a). $\alpha\text{PD-L1}$ weakly inhibited the tumor growth due to insufficient CTL infiltration in the 4T1 TNBC tumor as we reported previously.^[63] PDT alone by ICG or chemotherapy by ISPN moderately inhibited the tumor growth. Combination PDT and chemotherapy by ISPN+L showed improved antitumor performance for highly efficient tumor growth inhibition. In contrast,

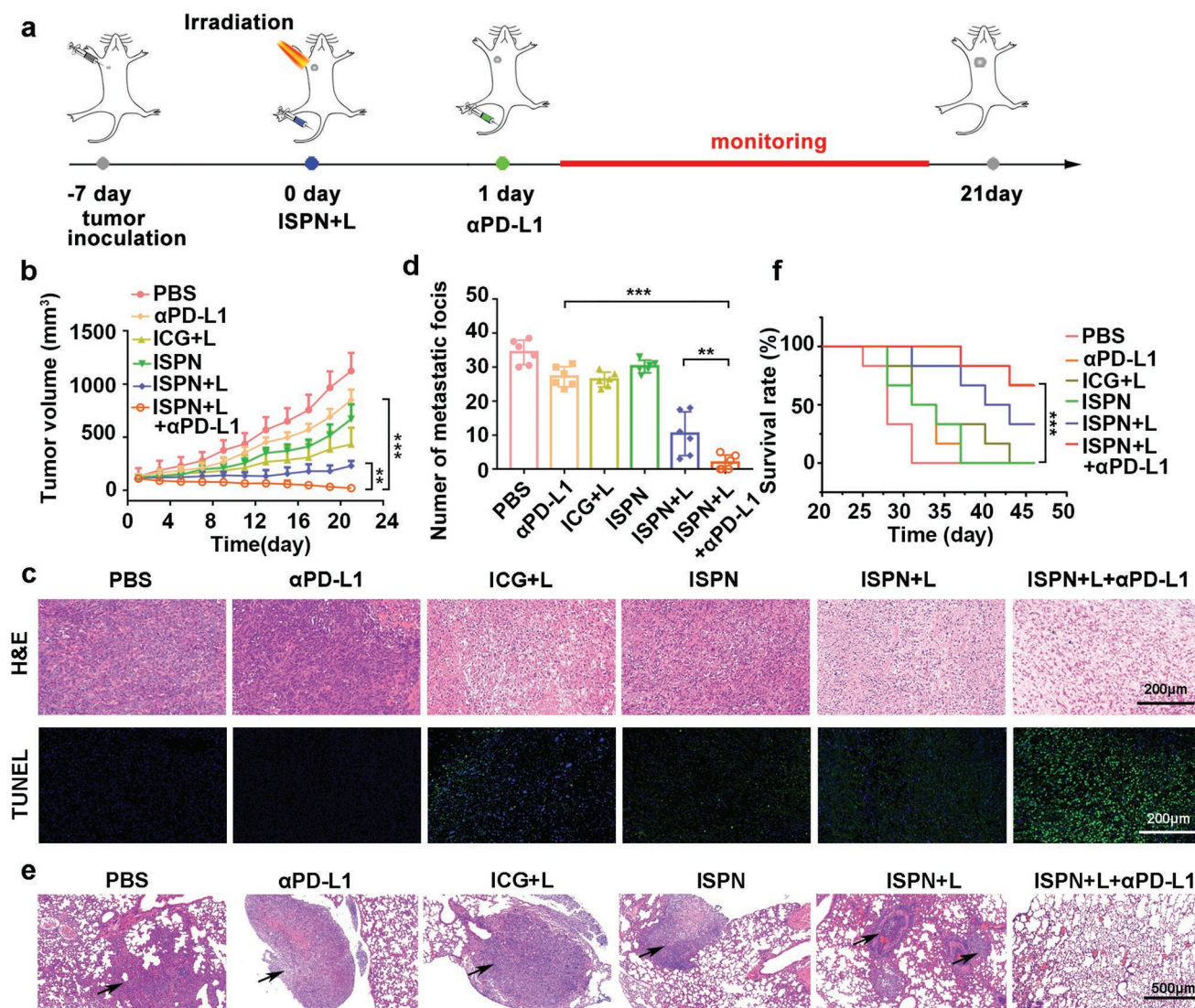


Figure 6. Antitumor performance of ISPN in combination with ICB therapy. a) Experimental schedule for ISPN-mediated combination therapy with α PD-L1; b) The tumor growth curves in 4T1-tumor-bearing mice following indicated treatments ($n = 6$, mean \pm s.d., $**p < 0.01$, $***p < 0.001$); c) H&E and TUNEL staining of the tumor section at the end of antitumor study (scale bars = 200 μ m); d) The number of lung metastatic nodules of 4T1 tumor bearing BALB/c mice examined at the end of the antitumor study ($n = 6$, mean \pm s.d., $**p < 0.01$, $***p < 0.001$); e) H&E staining of the lungs at the end of antitumor studies (the black arrows indicated the metastatic nodules, scale bar = 500 μ m); f) The survival rate of mice following indicated treatments ($n = 6$, mean \pm s.d., $**p < 0.01$, $***p < 0.001$).

the combination of α PD-L1 with ISPN+L highly efficiently suppressed 4T1 tumor growth (Figure 6b).

To rule out the influence of photothermal effect of ICG for tumor regression, 808 nm laser irradiation induced photothermal effect was monitored by measuring temperature elevation during the laser irradiation. Negligible photothermal effect was detected the PDT process, verifying the crucial role of PDT for tumor growth inhibition (Figure S5, Supporting Information). Haematoxylin and eosin (H&E) and terminal deoxynucleotidyl transferase dUTP nick end labeling (TUNEL) staining of the tumor sections further revealed obvious necrosis and apoptosis of the tumor cells in the ISPN+L+ α PD-L1 group (Figure 6c).

Metastasis is the leading cause of cancer-related human mortality; thus the lung metastasis of 4T1 tumor cells was

evaluated after the treatment. The number of lung metastatic nodules significantly decreased in the ISPN+L+ α PD-L1 group without obvious metastasis clones in the lungs as verified by H&E staining assay (Figure 6d,e). Moreover, 67% of mice in the ISPN+L+ α PD-L1 group survived while most mice receiving other treatments lost at the end of the antitumor study, suggesting combination immunotherapy by ISPN+L and α PD-L1 dramatically suppressed the distant metastasis of the tumor cells and prolonged the surveillance of the tumor-bearing mice (Figure 6f). The body weight of mice treated by ISPN+L and ICB blockade remained unaffected during the treatment, and no histopathological damage of the major organs (e.g., heart, liver, spleen, lung, and kidney) was found, suggesting good biosafety of the combination therapy (Figures S6 and S7, Supporting Information).

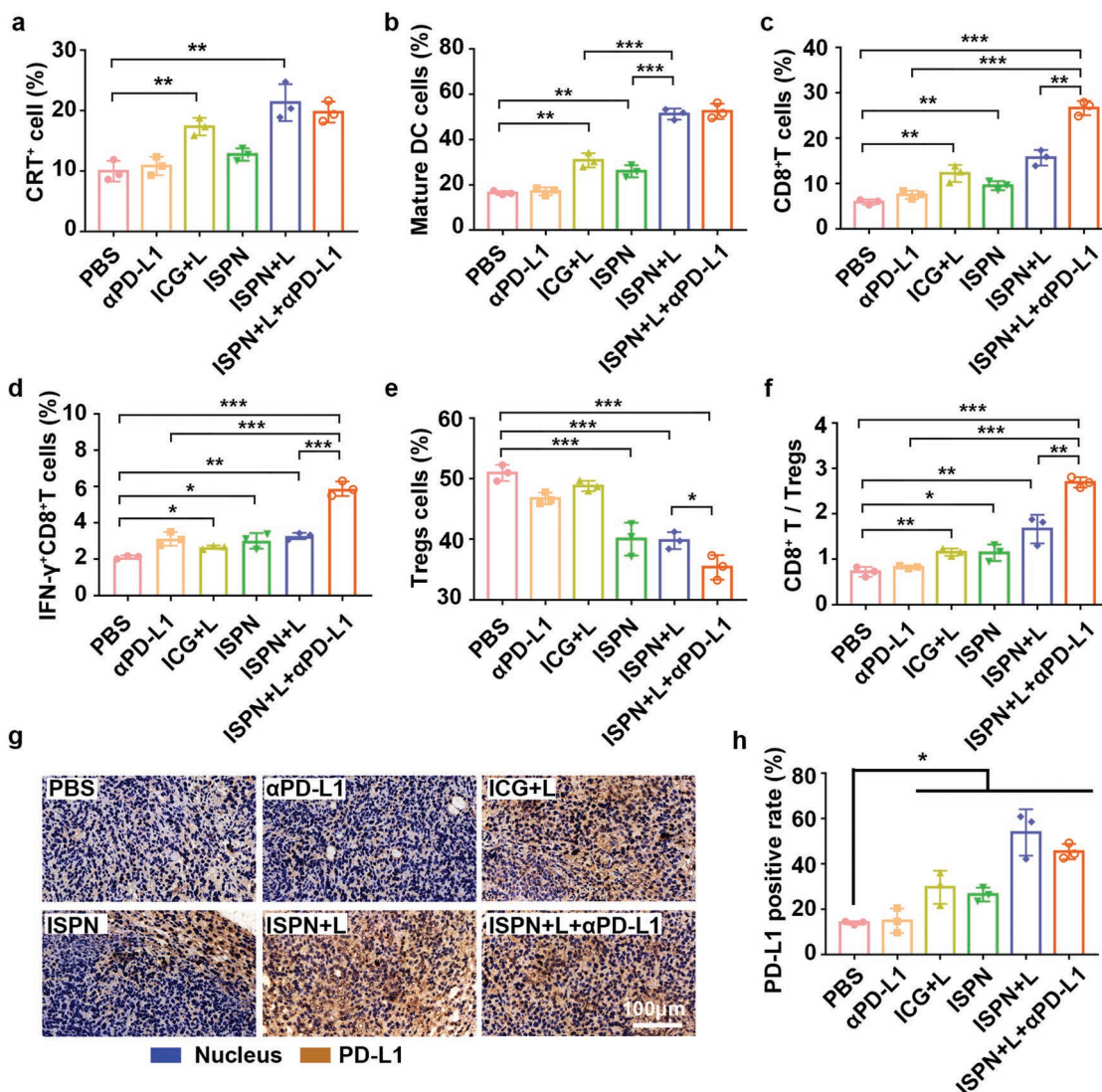


Figure 7. Antitumor immunity induced by ISPN in combination with α PD-L1 in vivo. a) intratumoral CRT exposure in vivo induced by ISPN; ISPN accelerated the DC maturation b), effector CD8⁺ T cells c), and IFN- γ ⁺ effector CD8⁺ T cells d) tumor infiltration within tumors; The intratumoral infiltration of T_{regs} e), and f) the CD8⁺ T cells to T_{regs} ratios calculated by dividing the data in (c) by that in (e); IHC analysis of intratumoral PD-L1 expression g) (scale bar = 100 μ m) and the PD-L1 positive rate in different groups h) (The data are expressed as mean \pm SD. * p < 0.05; ** p < 0.01; *** p < 0.001).

2.6. Antitumor Immune Response of Combination Immunotherapy

We next sought to elucidate the mechanism underlying the synergistic antitumor efficacy of ISPN and ICB therapy. Immunohistochemical (IHC) analysis revealed significant CRT expression on the surface of tumor cells after ISPN+L treatment (Figure S8, Supporting Information). The CRT expression of ISPN+L group was 2.1-fold higher than that of the PBS-treated control group (Figure 7a), suggesting ISPN-based chemotherapy and PDT efficiently induced ICD of the tumor cells in vivo.

DC maturation in the tumor-draining lymph nodes was then examined using flow cytometric measurement. PDT based on ICG and chemotherapy based on ISPN significantly facilitated DC maturation compared to the PBS group (Figure S9,

Supporting Information). The DC maturation rates reached to 51.3% when mice received the combination therapy based on ISPN and was 3.1-fold higher than that of control group, indicating ISPN could significantly enhance the tumor immunogenicity and DC maturation in lymph nodes (LNs) through combination therapy (Figure 7b).

The intratumoral infiltration of CTLs was investigated by flow cytometric measurement (Figure S10, Supporting Information). As shown in Figure 7c, mice receiving ISPN-based chemotherapy and PDT had more intratumoral CTLs infiltration than those receiving single therapy. Moreover, the combination of ISPN+L with α PD-L1 further promoted the intratumoral infiltration of CTLs up to 26.7%, which was 3.5-fold higher than that of single ICB therapy. Furthermore, the combination therapy of ICB and ISPN+L more efficiently promoted the intratumoral infiltration of interferon γ positive (IFN- γ) CTLs up to

5.9%, which was 1.8- and 1.9-fold higher than that of ISPN+L group and ICB group, respectively (Figure 7d, and Figure S11, Supporting Information).

T_{regs} is the main type of immunosuppressive T lymphocytes recruited by tumor cells to inactivate CTLs. T_{regs} infiltration in the tumor mass was thus evaluated by flow cytometric examination. The PBS group showed up to 51% intratumoral infiltration of T_{regs} , verifying ITM of the 4T1 tumor. The intratumoral T_{regs} dramatically decreased to 40% by ISPN treatment, which could be attributed to PTX-mediated killing of T_{regs} (Figure 7e and Figure S12, Supporting Information). Furthermore, the CTLs to T_{regs} ratio of the ISPN+L+ α PD-L1 group was 1.6-fold higher than that of the ISPN+L group, and 3.2-fold higher than that of the α PD-L1 group, respectively, verifying the T_{reg} elimination effect of PTX. These results indicated ISPN effectively elicited antitumor immune response in combination with ICB therapy by enhancing the tumor immunogenicity and overcoming ITM.

The elicitation of antitumor immunity was evaluated by examining intratumoral secretion of immune cytokines using enzyme-linked immunosorbent assays (ELISA). The intratumoral content of inflammatory cytokines including IFN- γ , TNF- α , and IL-6 dramatically increased both in ISPN+L group and ISPN+L+ α PD-L1 group, verifying the induction of antitumor immune response (Figure S13, Supporting Information).

Several groups including ours had demonstrated that upregulation of PD-L1 expression in the tumor tissue could sensitize the tumor cells to ICB therapy in vivo.^[64–66] IHC analysis showed that combination therapy based on ISPN resulted in high expression of PD-L1 in the tumor mass and the PD-L1 positive

rate was 3.2-fold higher than that of control group (Figure 7g,h). These results indicated that ISPN could promote the expression of PD-L1 and enhance the antitumor immune response of ICB therapy in TNBC to achieve improved therapeutic outcome.

To elucidate the mechanism underlying, we treated the tumor cells with IFN- γ , the dominant cytokine executes the antitumor function of CTLs. Both the western-blot assay and flow cytometric examination verified significant PD-L1 upregulation upon IFN- γ incubation for 24 h and an IFN- γ concentration of 100 ng mL⁻¹ (Figure S14, Supporting Information). According to the literature reports, this phenomenon could be most likely explained by IFN- γ -triggered activation of cyclin-dependent kinase 5 (CDK5), a highly active serine-threonine kinase in many cancers.^[67] Furthermore, several recent studies also proposed that IFN- γ elicit PD-L1 expression through the JAK-STAT pathway.^[68]

2.7. Tumor Recurrence Suppression by Combination Immunotherapy

To further demonstrate the potential of ISPN-mediated immunotherapy to prevent tumor recurrence, a secondary tumor model was established by rechallenging 4T1 tumor cells into the tumor-free mice surviving from ISPN+L+ α PD-L1 combination therapy. Untreated BALB/c mice were implanted with 4T1 tumor cells and set as the control group (Figure 8a). The pretreated animal group showed significantly delayed growth of the secondary 4T1 tumors with complete tumor eradication in 2 of 5 mice. In contrast, the 4T1 tumor grew quickly

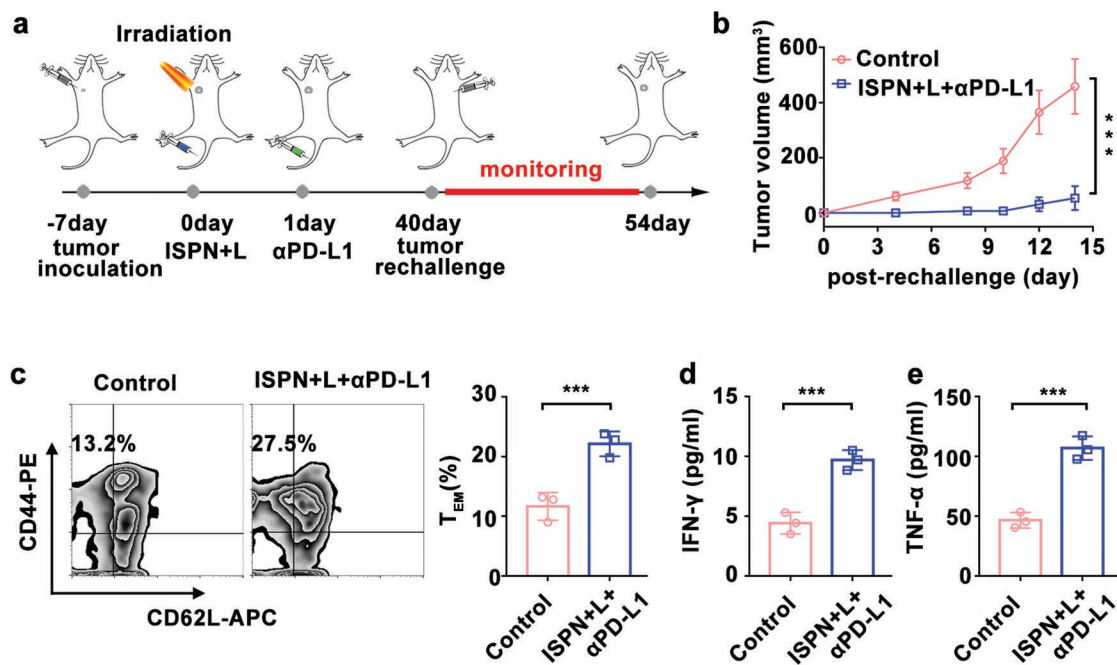


Figure 8. Tumor recurrence suppression of ISPN in combination with α PD-L1 in vivo. a) Schedule for ISPN-mediated combination therapy with α PD-L1 and tumor rechallenge through subcutaneously injecting 1×10^6 4T1 tumor cells 40 d post treatment; b) The rechallenged tumor growth curves in mice bearing 4T1 tumors following the indicated treatments ($n = 5$); c) Flow cytometric analysis of the frequency of T_{EM} in spleens (gated on $CD3^+ CD8^+$) the day before tumor re-challenge ($n = 3$); IFN- γ d) and TNF- α e) secretion in sera collected from 4T1 tumor-bearing mice 3 d post tumor rechallenging ($n = 3$) (The data are expressed as mean \pm SD. * $p < 0.05$; ** $p < 0.01$; *** $p < 0.001$).

in the control group (Figure 8b and Figure S15, Supporting Information), implying the potential of ISPN+L+ α PD-L1 to elicit durable antitumor immune response for long-term tumor regression.

The effector memory T cells (T_{EM}) play crucial roles in tumor recurrence prevention. We therefore examined the frequency of T_{EM} in the spleen by using flow cytometric examination. Figure 8c displayed that the T_{EM} of the ISPN+L+ α PD-L1 group significantly increased up to $22.1 \pm 2.1\%$, which was twofold higher than that of the PBS group. The concentration of IFN- γ and TNF- α in the sera significantly increased compared to the control group when mice in ISPN+L+ α PD-L1 group were rechallenged with tumor cells (Figure 8d,e). These results indicated that combination therapy by ISPN and α PD-L1 efficiently elicited antitumor immune response and immune memory effect for preventing tumor recurrence.

3. Conclusion

In this study, we demonstrated the preparation ICG-templated self-assemble nanoparticles of small molecular drugs. ISPN integrating ICG and PTX displayed elongated blood circulation in vivo and increased tumor accumulation in tumor-bearing mice than free ICG and PTX. ISPN efficiently elicited the antitumor immunity and promoted intratumoral infiltration of CTLs through PDT-induced ICD of the tumor cells in vitro and in vivo. Meanwhile, ISPN dramatically inhibited the recruitment of T_{regs} to relieve ITM. ISPN displayed cumulative antitumor performance to inhibit tumor growth and suppress lung metastasis in combination with ICB therapy. Moreover, we demonstrated that the combination of ISPN and ICB therapy induced long-term memory immune response to prevent tumor recurrence. Most importantly, ICG-templated self-assembly procedure could be readily extended to other small molecular drugs. Overall, this study might imply the promising potential of ICG-templated self-assembly strategy for the development of excipient-free nanomedicine and combination immunotherapy.

4. Experimental Section

Materials: ICG was purchased from J&K Chemical (Shanghai, China). PTX and all other small molecular drugs were purchased from Dalian Meilun Biotech CO., Ltd (Dalian, China). 3-(4, 5-dimethylthiazol-2-yl)-2,5-diphenyltetrazolium bromide (MTT) were purchased from Sigma-Aldrich (Shanghai, China). The ATP assay kit was purchased from Beyotime Biotechnology Co., Ltd (Nantong China). RPMI 1640 cell culture medium, fetal bovine serum (FBS), penicillin-streptomycin solution, and trypsin-EDTA solution were purchased from Gibco (Tulsa, OK). FoxP3 buffer set, anti-CD11c-FITC, anti-CD80-PE, anti-CD86-APC, anti-CD3-PerCP-Cy5.5, anti-CD4-FITC, anti-CD8-PE, anti-CD25-APC, anti-FoxP3-PE, and anti-IFN- γ -APC antibodies were all purchased from BioLegend, Inc. (San Diego, USA). Antibodies for Calprotectin (CRT), high mobility group B1 (HMGB-1) protein were purchased from Biosynthesis Biotechnology Inc. (Beijing, China). PD-L1 antibody were obtained from Abcam (UK). The ELISA Kits for IFN- γ , TNF- α , and IL-6 were purchased from Dakewe Biotech Co., Ltd. (Shenzhen, China). All other chemicals, if not mentioned, were analytical grade and obtained from SinoPharm Chemical Reagent Co., Ltd. (Shanghai, China).

Cell Lines: Murine 4T1 breast cancer cell line was obtained from the cell bank of the Chinese Academy of Sciences (Shanghai, China). The cells were cultured in complete RPMI 1640 cell culture medium containing 10% FBS, 2.5 g L^{-1} of glucose, 0.11 g L^{-1} of sodium pyruvate, 100 U mL^{-1} of penicillin G sodium, and $100 \mu\text{g mL}^{-1}$ of streptomycin sulfate. The cells were maintained at 37°C incubator at 5.0% CO_2 atmosphere.

Animals: Four-week-old female BALB/c mice and SD rats were obtained from the Shanghai Experimental Animal Center (Shanghai, China). All animal procedures were carried out under the guidelines approved by the Institutional Animal Care and Use Committee (IACUC) of the Shanghai Institute of Material Medica, Chinese Academy of Sciences.

Preparation of ISPN: The small molecular drug-loaded ICG nanoparticles were prepared through ICG-templated self-assembly of the small molecular drugs. Typically, 0.8 mg of PTX in 100 μL of DMSO solution was dropped into 1.0 mg mL^{-1} aqueous solution of ICG under consistent shaking for 15 min. Then the mixture was centrifuged at 15 000 g for 30 min to collect the pellet and resuspended in water solution. The free drug was removed by ultracentrifugation (molecular weight cut-off, MWCO 10 kDa). The resultant ISPN was dispersed in DI water.

Characterization of ISPN: The hydrodynamic diameter and zeta potential of ISPN were determined using DLS (Nanosizer, Malvern Instrument). The morphology of the nanoparticles was observed using TEM (JEOL, Japan). The drug loading ratio (DL) of PTX and ICG were measured using HPLC and fluorescence spectrophotometer, respectively. To investigate the interaction for ISPN formation, ISPN was incubated in the buffer solution of NaCl ($10 \times 10^{-3} \text{ M}$), urea ($10 \times 10^{-3} \text{ M}$), or SDS ($10 \times 10^{-3} \text{ M}$). The nanoparticles suspension was then examined by using UV-vis spectrophotometer, fluorescence spectrophotometer, and size change were examined using DLS, respectively.

Cellular Uptake and ROS Production In Vitro: To examine the intracellular uptake profile of ISPN, 2×10^4 4T1 cells were seeded on 24-well plate and then treated with ISPN at an ICG concentration of $1.0 \mu\text{g mL}^{-1}$, the cells were collected at the desired time interval to examine the intracellular fluorescence using flow cytometric measurement (FACS Caliber system, BD Biosciences, Oxford, UK).

To examine the photoactivity of ISPN nanoparticles in vitro, 2×10^4 of 4T1 cells were seeded on 24-well plate and then treated with ISPN at an ICG concentration of $1.0 \mu\text{g mL}^{-1}$ for 8 h. The cells were then irradiated with 808 nm laser for 0.5 min at photodensity of 1.0 W cm^{-2} . The cells were loaded with DCFH-DA before laser irradiation. The intracellular DCF fluorescence intensity was examined by flow cytometric measurement, respectively.

To visualize intracellular ROS generation in vitro, 2×10^4 of 4T1 cells were seeded on a live cell imaging glass bottom dish overnight. The cells were treated with ISPN at a final ICG concentration of $1.0 \mu\text{g mL}^{-1}$ for 8 h, and then irradiated with 808 nm laser at photodensity of 1.0 W cm^{-2} for 0.5 min. The cells were washed twice, loaded with DCFH-DA before the irradiation, stained with DAPI and examined by CLSM.

CRT Expression on the Surface of the Tumor Cells In Vitro: Surface expression of CRT on the tumor cells was investigated using flow cytometric measurement and immunofluorescence, respectively. Briefly, 4T1 cells in the 24-well tissue culture plate were incubated with ISPN at an ICG concentration of $1.0 \mu\text{g mL}^{-1}$ for 12 h. Then the cells were washed twice and irradiated with 808 nm laser (1.0 W cm^{-2}) for 30 s. The cells were washed twice with cold PBS 4 h postlaser irradiation, and fixed in 0.25% paraformaldehyde for 5 min. The cells were then incubated with primary antibody and Alexa488-conjugated monoclonal secondary antibody for 30 min. Finally, the surface expression of CRT was examined using flow cytometric measurement (FACS Caliber system, BD Biosciences, Oxford, UK).

To examine CRT expression using CLSM measurement, 4T1 cells were seeded on a live cell imaging glass bottom dish a density of 2×10^4 cells per well overnight and were incubated with ISPN at an ICG concentration of $1.0 \mu\text{g mL}^{-1}$ for 12 h. Then the cells were washed twice and irradiated with 808 nm laser (1 W cm^{-2}) for 30 s. The cells

were washed twice with cold PBS 4 h postlaser irradiation, and fixed in 4% paraformaldehyde for 20 min. The cells were then incubated with primary antibody and Alexa488-conjugated monoclonal secondary antibody for 30 min.

Intracellular HMGB1 Distribution: The intracellular HMGB1 distribution was examined by immunofluorescence analysis. Briefly, 4T1 cells were seeded on a live cell imaging glass bottom dish a density of 2×10^4 cells per well overnight and were incubated with ISPN at an ICG concentration of $1 \mu\text{g mL}^{-1}$ for 12 h. Then the cells were washed twice and irradiated with 808 nm laser (1.0 W cm^{-2}) for 30 s. The cells were fixed with 4% paraformaldehyde 24 h postlaser irradiation, and permeabilized with 0.1% Triton X-100 for 10 min, followed by incubation with primary antibody for 1 h, and then incubated with an Alexa Fluor 488-secondary antibody for 30 min after three cycles wash with PBS. The cells were stained with DAPI and examined by CLSM.

Extracellular ATP Secretion: Extracellular ATP secretion was tested using an ATP assay kit. Briefly, 4T1 cells were seeded on a live cell imaging glass bottom dish a density of 2×10^4 cells per well overnight and were incubated with ISPN at an ICG concentration of $1.0 \mu\text{g mL}^{-1}$ for 12 h. Then the cells were washed twice and irradiated with 808 nm laser (1.0 W cm^{-2}) for 30 s. The cell culture medium was collected 12 h post treatment, and the ATP content was tested using an ATP assay kit according to manufacturer's instructions.

DC Maturation In Vitro: To investigate DC maturation in vitro, bone marrow-derived dendritic cells (BMDCs) were generated from the bone marrow of 8 week old BALB/c mice. Immature DC cells were cocultured with ISPN-pretreated 4T1 cells for 24 h. After staining with anti-CD11c-FITC, anti-CD80-PE, and anti-CD86-APC antibodies, the DC cells were analyzed using flow cytometry.

The Cytotoxicity and Phototoxicity In Vitro: To examine the synergistic antitumor effect of chemotherapy and PDT of ISPN in vitro, 4T1 cells were seeded in the 96-well plate at a density of 3500 cells per well in $100 \mu\text{L}$ of medium. After 12 h preincubation, the cells were incubated with ISPN or ICG at an identical ICG concentration gradient for 12 h. The cells were washed twice and irradiated with 808 nm laser (1.0 W cm^{-2}) for 30 s and continue to incubation. 12 h later, the cell viability was tested using MTT assay.

Pharmacokinetics Profile and Biodistribution of ISPN In Vivo: To investigate the pharmacokinetics of the nanoparticles, SD rats (female, 4–5 weeks, $180 \pm 10 \text{ g}$, Shanghai Experimental Animal Center, Shanghai, China) were i. v. injected with ISPN or PTX solution at an identical PTX dose of 5 mg kg^{-1} . Blood samples were collected at 5, 15, 30 min, 1, 2, 4, 8, 12, and 24 h postinjection. The blood concentration of PTX was quantitatively examined using HPLC.

To investigate ISPN distribution in vivo, 4T1 tumor-bearing BALB/c mice were i. v. injected with ISPN, ICG, or PTX solution at an identical ICG dose of 0.5 mg kg^{-1} and PTX dose of 5.0 mg kg^{-1} , respectively, when the tumor size reached 100 mm^3 . NIR fluorescence imaging in vivo were carried out with an IVIS imaging system (Xenogen, Alameda, CA). The mice were sacrificed to collect the major tissues 24 h postinjection for determining the fluorescence intensity and drug distribution of nanoparticles.

To detect laser irradiation-induced ROS generation in vivo, 4T1 tumor bearing BALB/c mice were i.v. injected with ISPN, ICG, or PTX at an identical ICG dose of 0.5 mg kg^{-1} when the tumor size reached 100 mm^3 . The tumors were locally irradiated with 808 nm laser at photodensity of 2.0 W cm^{-2} for 5 min. The tumor tissues were harvested and frozen sectioned to examine intratumoral ROS generation by CLSM.

Antitumor Effect In Vivo: The antitumor effect of combination therapy based on ISPN and ICB was performed using a 4T1 murine TNBC tumor model. The subcutaneous 4T1 tumors were established by s.c. injecting 1×10^6 4T1 cells into the right mammary gland. The tumor-bearing mice were randomly divided into six groups ($n = 6$) when the tumor volume reached 100 mm^3 . The mice were then treated with PBS, ICG, or ISPN at an ICG dose of 0.5 mg kg^{-1} and PTX dose of 5 mg kg^{-1} , respectively. The mice were irradiated with 808 nm laser for 5 min at photodensity of 2.0 W cm^{-2} . $\alpha\text{PD-L1}$ was i. v. injected at a dose of 1.0 mg kg^{-1} 24 h postlaser irradiation. The tumor volume was calculated by using the formula

$$V = L \times W \times W/2 (L, \text{ the longest dimension; } W, \text{ the shortest dimension}) \quad (1)$$

The major organs (tumors, heart, liver, spleen, and kidneys) were harvested, fixed in 4% formalin solution, dehydrated and subjected to H&E staining.

CRT Expression In Vivo: To examine treatment-induced CRT expression in vivo, 4T1-tumor bearing BALB/c mice were treated with various formulations. The tumors were harvested 3 d post treatment, fixed in 4% formalin and subjected to IHC staining.

DC Maturation In Vivo: To examine DC maturation in vivo, 4T1 tumor-bearing BALB/c mice were treated with various formulations. The inguinal LNs were harvested 3 d post treatment. The frequency of DC maturation in the LNs was then examined by flow cytometric measurement.

Intratumoral Infiltration of T Lymphocytes: To examine the intratumoral infiltration of T lymphocytes, the tumor xenografts were harvested 3 d post treatment and cut into small pieces, immersed in the solution of 1 mg mL^{-1} collagenase IV and 0.2 mg mL^{-1} DNase I for 45 min at 37°C . The single cell suspension was stained with fluorescent-labeled antibody according to manufacturer's protocols. For the analysis of CTLs ($\text{CD3}^+\text{CD4}^+\text{CD8}^+$), the T lymphocytes were stained with anti-CD3-PerCP-Cy5.5, anti-CD4-FITC, anti-CD8-PE, and anti-IFN- γ -APC antibodies according to manufacturer's protocols. To analyze the frequency of T_{regs} ($\text{CD3}^+\text{CD4}^+\text{CD25}^+\text{Foxp3}^+$), the lymphocytes were stained with anti-CD3-PerCP-Cy5.5, anti-CD4-FITC, anti-CD25-APC, and anti-FoxP3-PE according to the manufacturer's protocols. The cells were analyzed by flow cytometric measurement.

Cytokine Secretion in the Tumor Tissues: To examine the intratumoral secretion of IFN- γ , TNF- α , and IL-6 cytokines, the tumors were homogenized and centrifuged to harvest the supernatant. Cytokines in the supernatant were measured using an ELISA kit according to the manufacturer's instructions.

Tumor Recurrence Prevention: 4T1-tumor bearing BALB/c mice were treated with the combination therapy based on ISPN and PD-L1 antibody. The surviving mice were reinjected 1×10^6 4T1 cells in the right back 30 d post the treatment. The volume of reimplanted tumors was monitored to examine the tumor recurrence.

Analysis of Memory T Lymphocytes in the Spleen: The spleens from the surviving mice were harvested 30 d post treatment and pressed gently to obtain a single cell suspension solution using a syringe piston. Then the single cells were stained with fluorescent-labeled antibody according to the manufacturer's protocols. For the analysis of T_{EM} ($\text{CD3}^+\text{CD8}^+\text{CD44}^+\text{CD62L}^-$), the T lymphocytes were stained with anti-CD3-FITC, anti-CD8-PerCP-Cy5.5, anti-CD62L-APC, anti-CD44-PE according to the manufacturer's protocols.

Cytokine Secretion in the Sera: Blood from mice treated with different therapeutics was collected and centrifuge to obtain sera. Cytokines in the sera were measured using an ELISA kit according to the manufacturer's instructions.

Statistical Analysis: Statistical evaluations of data were performed using the Student's *t*-test. All results were expressed as mean \pm standard error unless otherwise noted. * $P < 0.05$, ** $P < 0.01$, *** $P < 0.001$.

Supporting Information

Supporting Information is available from the Wiley Online Library or from the author.

Acknowledgements

B.F., Z.N., and B.H. contributed equally to this work. Financial supports from the National Natural Science Foundation of China (Nos. 31671024, 51873228, 31622025, and 81521005), the Strategic Priority Research Program of CAS (No. XDA12050307), and the Youth Innovation Promotion Association of Chinese Academy of Sciences (No. 2014218)

are gratefully acknowledged. All animal procedures were carried out under the guidelines approved by the Institutional Animal Care and Use Committee (IACUC) of the Shanghai Institute of Materia Medica, Chinese Academy of Sciences.

Conflict of Interest

The authors declare no conflict of interest.

Keywords

immune checkpoint blockade, immunogenic cell death, immunotherapy, self-assemble, triple negative breast cancer

Received: August 12, 2019

Revised: September 25, 2019

Published online:

- [1] D. Samanta, Y. Park, X. Ni, H. Li, C. A. Zahnow, E. Gabrielson, F. Pan, G. L. Semenza, *Proc. Natl. Acad. Sci. USA* **2018**, *115*, E1239.
- [2] D. Merino, T. S. Weber, A. Serrano, F. Vaillant, K. Liu, B. Pal, L. Di Stefano, J. Schreuder, D. Lin, Y. Chen, M. L. Asselin-Labat, T. N. Schumacher, D. Cameron, G. K. Smyth, A. T. Papenfuss, G. J. Lindeman, J. E. Visvader, S. H. Naik, *Nat. Commun.* **2019**, *10*, 766.
- [3] L. Carey, E. Winer, G. Viale, D. Cameron, L. Gianni, *Nat. Rev. Clin. Oncol.* **2010**, *7*, 683.
- [4] B. Feng, Z. Xu, F. Zhou, H. Yu, Q. Sun, D. Wang, Z. Tang, H. Yu, Q. Yin, Z. Zhang, Y. Li, *Nanoscale* **2015**, *7*, 14854.
- [5] L. Zhang, C. H. Zhang, Z. Y. Yang, M. He, L. J. Zhang, S. Ezzat, X. Liang, *OncoTargets Ther.* **2017**, *10*, 5459.
- [6] Y. M. Kirova, Y. De Rycke, L. Gambotti, J.-Y. Pierga, B. Asselain, *Br. J. Cancer* **2008**, *98*, 870.
- [7] A. Ribas, J. D. Wolchok, *Science* **2018**, *359*, 1350.
- [8] H. Yousefi, J. D. Yuan, M. Keshavarz-Fathi, J. F. Murphy, N. Rezaei, *Expert Rev. Clin. Immunol.* **2017**, *13*, 1001.
- [9] S. L. Topalian, C. G. Drake, D. M. Pardoll, *Cancer Cell* **2015**, *27*, 450.
- [10] S. Chretien, I. Zerdes, J. Bergh, A. Matikas, T. Foukakis, *Cancers* **2019**, *11*, 628.
- [11] N. D'Abreo, S. Adams, *Nat. Rev. Clin. Oncol.* **2019**, *16*, 399.
- [12] M. E. Valsecchi, *N. Engl. J. Med.* **2015**, *373*, 1270.
- [13] J. S. O'Donnell, M. W. L. Teng, M. J. Smyth, *Nat. Rev. Clin. Oncol.* **2019**, *16*, 151.
- [14] T. K. Kim, R. S. Herbst, L. P. Chen, *Trends Immunol.* **2018**, *39*, 624.
- [15] X. J. Liu, Y. Pu, K. Cron, L. F. Deng, J. Kline, W. A. Frazier, H. R. Xu, H. Peng, Y. X. Fu, M. M. Xu, *Nat. Med.* **2015**, *21*, 1209.
- [16] C. Sheridan, *Nat. Biotechnol.* **2015**, *33*, 321.
- [17] M. J. Smyth, S. F. Ngiew, A. Ribas, M. W. L. Teng, *Nat. Rev. Clin. Oncol.* **2016**, *13*, 143.
- [18] W. Song, J. Kuang, C. X. Li, M. K. Zhang, D. W. Zheng, X. Zeng, C. J. Liu, X. Z. Zhang, *ACS Nano* **2018**, *12*, 1978.
- [19] P. Kadiyala, D. Li, F. M. Nunez, D. Altschuler, R. Doherty, R. Kuai, M. Yu, N. Kamran, M. Edwards, J. J. Moon, P. R. Lowenstein, M. G. Castro, A. Schwendeman, *ACS Nano* **2019**, *13*, 1365.
- [20] P. Gotwals, S. Cameron, D. Cipolletta, V. Cremasco, A. Crystal, B. Hewes, B. Mueller, S. Quarantino, C. Sabatos-Peyton, L. Petruzzelli, J. A. Engelman, G. Dranoff, *Nat. Rev. Cancer* **2017**, *17*, 286.
- [21] D. S. Wilson, S. Hirose, M. M. Racz, L. Bonilla-Ramirez, L. Jeanbart, R. Wang, M. Kwissa, J. F. Franetich, M. A. S. Broggi, G. Diaceri, X. Quaglia-Thermes, D. Mazier, M. A. Swartz, J. A. Hubbell, *Nat. Mater.* **2019**, *18*, 175.
- [22] Q. Chen, C. Wang, X. Zhang, G. Chen, Q. Hu, H. Li, J. Wang, D. Wen, Y. Zhang, Y. Lu, G. Yang, C. Jiang, J. Wang, G. Dotti, Z. Gu, *Nat. Nanotechnol.* **2019**, *14*, 89.
- [23] S. Yu, C. Wang, J. Yu, J. Wang, Y. Lu, Y. Zhang, X. Zhang, Q. Hu, W. Sun, C. He, X. Chen, Z. Gu, *Adv. Mater.* **2018**, *30*, 1801527.
- [24] G. Yang, L. Xu, J. Xu, R. Zhang, G. Song, Y. Chao, L. Feng, F. Han, Z. Dong, B. Li, Z. Liu, *Nano Lett.* **2018**, *18*, 2475.
- [25] C. Wang, J. Q. Wang, X. D. Zhang, S. J. Yu, D. Wen, Q. Y. Hu, Y. Q. Ye, H. Bomba, X. L. Hu, Z. Liu, G. Dotti, Z. Gu, *Sci. Transl. Med.* **2018**, *10*, eaan3682.
- [26] Y. Min, K. C. Roche, S. Tian, M. J. Eblan, K. P. McKinnon, J. M. Caster, S. Chai, L. E. Herring, L. Zhang, T. Zhang, J. M. DeSimone, J. E. Tepper, B. G. Vincent, J. S. Serody, A. Z. Wang, *Nat. Nanotechnol.* **2017**, *12*, 877.
- [27] Q. Xiong, G. Y. Lee, J. Ding, W. Li, J. Shi, *Nano Res.* **2018**, *11*, 5281.
- [28] Y. Mi, C. T. Hagan, B. G. Vincent, A. Z. Wang, *Adv. Sci.* **2019**, *6*, 1801847.
- [29] Y. Lv, C. Xu, X. Zhao, C. Lin, X. Yang, X. Xin, L. Zhang, C. Qin, X. Han, L. Yang, W. He, L. Yin, *ACS Nano* **2018**, *12*, 1519.
- [30] C. F. Xu, S. Iqbal, S. Shen, Y. L. Luo, X. Yang, J. Wang, *Small* **2019**, *15*, 1900055.
- [31] J. E. Chung, S. Tan, S. J. Gao, N. Yongvongsoontorn, S. H. Kim, J. H. Lee, H. S. Choi, H. Yano, L. Zhuo, M. Kurisawa, J. Y. Ying, *Nat. Nanotechnol.* **2014**, *9*, 907.
- [32] R. Xing, Q. Zou, C. Yuan, L. Zhao, R. Chang, X. Yan, *Adv. Mater.* **2019**, *31*, 1900822.
- [33] J. Park, B. Sun, Y. Yeo, *J. Controlled Release* **2017**, *263*, 90.
- [34] K. Liu, R. Xing, Q. Zou, G. Ma, H. Mohwald, X. Yan, *Angew. Chem., Int. Ed.* **2016**, *55*, 3036.
- [35] Z. Wei, P. Liang, J. Xie, C. Song, C. Tang, Y. Wang, X. Yin, Y. Cai, W. Han, X. Dong, *Chem. Sci.* **2019**, *10*, 2778.
- [36] R. Zhang, R. Xing, T. Jiao, K. Ma, C. Chen, G. Ma, X. Yan, *ACS Appl. Mater. Interfaces* **2016**, *8*, 13262.
- [37] B. Feng, F. Zhou, W. Lu, D. Wang, T. Wang, C. Luo, H. Wang, Y. Li, H. Yu, *Biomater. Sci.* **2017**, *5*, 1522.
- [38] X. Xu, P. E. Saw, W. Tao, Y. Li, X. Ji, S. Bhasin, Y. Liu, D. Ayyash, J. Rasmussen, M. Huo, J. Shi, O. C. Farokhzad, *Adv. Mater.* **2017**, *29*, 1700141.
- [39] Q. Zou, M. Abbas, L. Zhao, S. Li, G. Shen, X. Yan, *J. Am. Chem. Soc.* **2017**, *139*, 1921.
- [40] J. Bhattacharyya, J. J. Bellucci, I. Weitzhandler, J. R. McDaniel, I. Spasojevic, X. Li, C. C. Lin, J. T. Chi, A. Chilkoti, *Nat. Commun.* **2015**, *6*, 7939.
- [41] X. P. Duan, C. Chan, W. B. Lin, *Angew. Chem., Int. Ed.* **2019**, *58*, 670.
- [42] A. P. Castano, P. Mroz, M. R. Hamblin, *Nat. Rev. Cancer* **2006**, *6*, 535.
- [43] F. Zhou, B. Feng, H. Yu, D. Wang, T. Wang, Y. Ma, S. Wang, Y. Li, *Adv. Mater.* **2019**, *31*, 1805888.
- [44] Z. K. Chen, L. L. Liu, R. J. Liang, Z. Y. Luo, H. M. He, Z. H. Wu, H. Tian, M. B. Zheng, Y. F. Ma, L. T. Cai, *ACS Nano* **2018**, *12*, 8633.
- [45] M. Obeid, A. Tesniere, F. Chiringhelli, G. M. Fimia, L. Apetoh, J. L. Perfettini, M. Castedo, G. Mignot, T. Panaretakis, N. Casares, D. Metivier, N. Larochette, P. van Endert, F. Ciccocanti, M. Piacentini, L. Zitvogel, G. Kroemer, *Nat. Med.* **2007**, *13*, 54.
- [46] F. Chiringhelli, L. Apetoh, A. Tesniere, L. Aymeric, Y. T. Ma, C. Ortiz, K. Vermaelen, T. Panaretakis, G. Mignot, E. Ullrich, J. L. Perfettini, F. Schlemmer, E. Tasdemir, M. Uhl, P. Genin, A. Civas, B. Ryffel, J. Kanellopoulos, J. Tschopp, F. Andre, R. Lidereau, N. M. McLaughlin, N. M. Haynes, M. J. Smyth, G. Kroemer, L. Zitvogel, *Nat. Med.* **2009**, *15*, 1170.
- [47] B. Feng, F. Zhou, B. Hou, D. Wang, T. Wang, Y. Fu, Y. Ma, H. Yu, Y. Li, *Adv. Mater.* **2018**, *30*, 1803001.

- [48] K. G. Anderson, I. M. Stromnes, P. D. Greenberg, *Cancer Cell* **2017**, *31*, 311.
- [49] H. Zhong, B. Han, I. L. Tourkova, A. Lokshin, A. Rosenbloom, M. R. Shurin, G. V. Shurin, *Clin. Cancer Res.* **2007**, *13*, 5455.
- [50] W. J. Shan, H. P. Zheng, G. F. Fu, C. F. Liu, Z. Z. Li, Y. H. Ye, J. Zhao, D. Xu, L. P. Sun, X. Wang, X. L. Chen, S. L. Bi, L. Ren, G. Fu, *Nano Lett.* **2019**, *19*, 1719.
- [51] L. Voorwerk, M. Slagter, H. M. Horlings, K. Sikorska, K. K. van de Vijver, M. de Maaker, I. Nederlof, R. J. C. Kluin, S. Warren, S. Ong, T. G. Wiersma, N. S. Russell, F. Lalezari, P. C. Schouten, N. A. M. Bakker, S. L. C. Ketelaars, D. Peters, C. A. H. Lange, E. van Werkhoven, H. van Tinteren, I. A. M. Mandjes, I. Kemper, S. Onderwater, M. Chalabi, S. Wilgenhof, J. Haanen, R. Salgado, K. E. de Visser, G. S. Sonke, L. F. A. Wessels, S. C. Linn, T. N. Schumacher, C. U. Blank, M. Kok, *Nat. Med.* **2019**, *25*, 920.
- [52] J. Zhao, Z. Xiao, T. Li, H. Chen, Y. Yuan, Y. A. Wang, C. H. Hsiao, D. S. Chow, W. W. Overwijk, C. Li, *ACS Nano* **2018**, *12*, 9881.
- [53] R. Kuai, W. Yuan, S. Son, J. Nam, Y. Xu, Y. Fan, A. Schwendeman, J. J. Moon, *Sci. Adv.* **2018**, *4*, eaao1736.
- [54] R. S. Riley, C. H. June, R. Langer, M. J. Mitchell, *Nat. Rev. Drug Discovery* **2019**, *18*, 175.
- [55] D. Banerjee, A. Cieslar-Pobuda, G. H. Zhu, E. Wiechec, H. K. Patra, *Trends Pharmacol. Sci.* **2019**, *40*, 403.
- [56] L. Zhang, K. Dermawan, M. Jin, R. Liu, H. Zheng, L. Xu, Y. Zhang, Y. Cai, Y. Chu, S. Xiong, *Clin. Immunol.* **2008**, *129*, 219.
- [57] A. Javeed, M. Ashraf, A. Riaz, A. Ghafoor, S. Afzal, M. M. Mukhtard, *Eur. J. Pharm. Sci.* **2009**, *38*, 283.
- [58] Q. Chen, J. Chen, Z. Yang, J. Xu, L. Xu, C. Liang, X. Han, Z. Liu, *Adv. Mater.* **2019**, *31*, 1802228.
- [59] W. Yang, G. Zhu, S. Wang, G. Yu, Z. Yang, L. Lin, Z. Zhou, Y. Liu, Y. Dai, F. Zhang, Z. Shen, Y. Liu, Z. He, J. Lau, G. Niu, D. O. Kiesewetter, S. Hu, X. Chen, *ACS Nano* **2019**, *13*, 3083.
- [60] Y. Li, N. Chen, M. Palmisano, S. Zhou, *Mol. Pharmaceut.* **2015**, *12*, 1308.
- [61] B. Feng, B. Hou, Z. Xu, M. Saeed, H. Yu, Y. Li, *Adv. Mater.* **2019**, 1902960.
- [62] D. Wang, T. Wang, H. Yu, B. Feng, L. Zhou, F. Zhou, B. Hou, H. Zhang, M. Luo, Y. Li, *Sci. Immunol.* **2019**, *4*, eaau6584.
- [63] K. Muro, H. C. Chung, V. Shankaran, R. Geva, D. Catenacci, S. Gupta, J. P. Eder, T. Golan, D. T. Le, B. Burtness, A. J. McRee, C. C. Lin, K. Pathiraja, J. Lunceford, K. Emancipator, J. Juco, M. Koshiji, Y.-J. Bang, *Lancet Oncol.* **2016**, *17*, 717.
- [64] M. Reck, D. Rodríguez-Abreu, A. G. Robinson, R. N. Hui, T. Csőszi, A. Fülöp, M. Gottfried, N. Peled, A. Tafreshi, S. Cuffe, M. O'Brien, S. Rao, K. Hotta, M. A. Leiby, G. M. Lubiniecki, Y. Shentu, R. Rangwala, J. R. Brahmer, *N. Engl. J. Med.* **2016**, *375*, 1823.
- [65] P. N. Aguiar Jr., R. A. De Mello, P. Hall, H. Tadokoro, G. de Lima, *Immunotherapy* **2017**, *9*, 499.
- [66] R. D. Dorand, J. Nthale, J. T. Myers, D. S. Barkauskas, S. Avril, S. M. Chirieleison, T. K. Pareek, D. W. Abbott, D. S. Stearns, J. J. Letterio, A. Y. Huang, A. Petrosiute, *Science* **2016**, *353*, 399.
- [67] M. Cerezo, R. Guemiri, S. Druillennec, I. Girault, H. Malka-Mahieu, S. Shen, D. Allard, S. Martineau, C. Welsch, S. Agoussi, C. Estrada, J. Adam, C. Libenciuc, E. Routier, S. Roy, L. Désaubry, A. M. Eggermont, N. Sonenberg, J. Y. Scoazec, A. Eychène, S. Vagner, C. Robert, *Nat. Med.* **2018**, *24*, 1877.
- [68] A. Garcia-Diaz, D. S. Shin, B. H. Moreno, J. Saco, H. Escuin-Ordinas, G. A. Rodriguez, J. M. Zaretsky, L. Sun, W. Hugo, X. Wang, G. Parisi, C. P. Saus, D. Y. Torrejon, T. G. Graeber, B. C. Anduix, S. Hu-Lieskovan, R. Damaoiseaux, R. S. Lo, A. Ribas, *Cell Rep.* **2017**, *19*, 1189.